Phase-Diverse Coherent Diffractive Imaging: High Sensitivity with Low Dose

Corey T. Putkunz, Jesse N. Clark, David J. Vine, Garth J. Williams, Mark A. Pfeifer, Eugeniu Balaur, Ian McNulty, Keith A. Nugent, and Andrew G. Peele

Phase diverse coherent diffractive imaging:
high sensitivity with low dose

Corey T. Putkunz,[1,3] Jesse N. Clark,[1,3] David J. Vine,[2,3] Garth J. Williams,[2,3] Mark A. Pfeifer,[1,3] Eugeniu Balaur,[1,3] Ian McNulty,[4] Keith A. Nugent,[2,3] and Andrew G. Peele[1,3,*]

[1]*Department of Physics, La Trobe University, Victoria 3086, Australia*
[2]*School of Physics The University of Melbourne, Victoria 3010, Australia*
[3]*Australian Research Council Centre of Excellence for Coherent X-Ray Science*
[4]*Advanced Photon Source, Argonne National Laboratory, Argonne, Illinois 60439, USA*

This paper demonstrates that coherent diffractive imaging (CDI), in combination with phase-diversity methods, provides reliable and artefact free high-resolution images. Here, using X-rays, experimental results show a threefold improvement in the available image contrast. Furthermore, in conditions requiring low imaging dose, it is demonstrated that phase diverse CDI provides a factor of two improvement in comparison to previous CDI techniques.

Coherent diffractive imaging (CDI) methods are rapidly emerging as a powerful technique for the microscopy of materials and biological specimens using both X-rays [1] and electrons [2]. The principle behind CDI is a recognition that a coherent diffraction pattern of a finite isolated object has an almost unique relationship with the object [3], provided critical sampling conditions are met [4]. If it is possible to find an object distribution consistent with both the known physical extent of the object and its coherent diffraction pattern, then with a high degree of confidence one can be assured the reconstruction is correct. The correct distribution is typically obtained using iterative methods [5].

The adaptation of CDI to image extended samples was made possible by recognising that an illumination which is finite in extent also satisfies the conditions for a unique solution [6, 7]. The method of ptychography, an approach initially proposed for electron imaging [8], uses a multitude of diffraction patterns from overlapping regions to recover the distribution of an extended object. The method was first demonstrated using the direct methods of phase-space deconvolution [9]. Iterative methods were subsequently developed [10].

In this letter we present phase diverse CDI, in which diffraction data from a diverse set of illuminating wavefields are used to reconstruct a common object. Phase-diversity was originally introduced as a method of perturbing known aberrations in two or more optical images to identify a common object [11]. Ptychography conforms to the broad method of phase-diversity, however, there are many other possibilities such as changes in propagation distance [12], through focus series methods [13], and, indeed, other forms of phase structure [14].

Suppose that the object we wish to image is described via the complex refractive index $\boldsymbol{n}(\boldsymbol{r}_s) = 1 - \delta(\boldsymbol{r}_s) + i\beta(\boldsymbol{r}_s)$, where $\boldsymbol{r}_s = (\boldsymbol{\rho}_s, z_s)$ is the three dimensional sample coordinate. We assume that the wavefield in-

cident on the object is described by $\psi_0(\boldsymbol{\rho}_s)$, which obeys the paraxial approximation. In the projection approximation, the exit wavefield of the object can be calculated via the product of the incident illumination, and the integral through the object, known as the complex transmission function; for a weak object: $T(\boldsymbol{\rho}_s) \simeq \exp\left[-ik\int_{z_s} \delta(\boldsymbol{\rho}_s, z_s) - i\beta(\boldsymbol{\rho}_s, z_s)dz_s\right]$, where $k = 2\pi/\lambda$.

The measured intensity in the far field at the detector, $I(\boldsymbol{\rho}_d)$, as described by the Fourier transform of the auto-correlation function, is proportional to the squared amplitude of the wavefield at the detector plane via $|\hat{\psi}(\boldsymbol{\rho}_d)|^2 \propto I(\boldsymbol{\rho}_d)$, where $\boldsymbol{\rho}_d$ is the planar detector coordinate. In the far field $\hat{\psi}(\boldsymbol{\rho}_d)$ may be iteratively solved for the exit surface wave of the object when using sufficient *a priori* constraints. Typically either the illuminating probe, or the object must be finite in extent. Phase curvature has been shown to provide reliable convergence characteristics [15], and has allowed the imaging of extended objects in 2D [6] and 3D [16]. Additional information for the solution can be provided by acquiring diffraction data from different forms of illumination. That is, to acquire sets of data, $I^j(\boldsymbol{\rho}_d)$, of the form:

$$I^j(\boldsymbol{\rho}_d) \propto \left| \int T(\boldsymbol{\rho}_s)\psi_j(\boldsymbol{\rho}_s) \exp\left[-\frac{2\pi i \boldsymbol{\rho}_d \cdot \boldsymbol{\rho}_s}{\lambda z_D}\right] d\boldsymbol{\rho}_s \right|^2 \quad (1)$$

where $\boldsymbol{\rho}_s$ is the planar sample coordinate and z_D is the propagation distance between the two planes.

The set of ψ_j defines the level of diversity in the effective illumination profile on the sample. This is essentially a form of the phase-diversity methods developed in adaptive optics for astronomy. One can use translational diversity, such as in ptychography, in which the illumination is translated in some way across the sample [17]. That is, $\psi_j(\boldsymbol{\rho}_s) = \psi_0(\boldsymbol{\rho}_s - \boldsymbol{\rho}_j)$, where we define $\boldsymbol{\rho}_j$ as the lateral displacement vector of the jth data set.

However, the concept of phase-diversity allows more than lateral translation of the illumination on the sample. Here we also consider the introduction of an
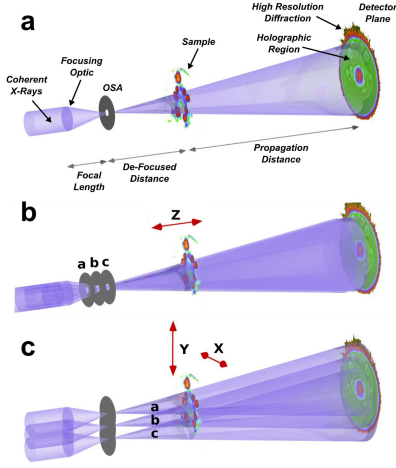
* a.peele@latrobe.edu.au

FIG. 1. A typical phase divers CDI experimental geometry. Coherent planar X-rays illuminate a Fresnel zone-plate (FZP) or alternate focusing optic. If a FZP is used, a small ($10 \ \mu$m) order sorting aperture (OSA) is used to remove high order diffraction. The arrangement here allows variation in longitudinal (z) and transverse (x and y) position, shown in (b) and (c) respectively.

additional phase curvature to the incident wavefield: $\exp\left[i\pi\rho_s^2/\lambda z_j\right]$, where z_j denotes a change in curvature for the jth data set, an approach that we will call longitudinal-diversity. Phase-diversity configurations are illustrated in Fig. 1 in the case where ψ_0 is the diverging wave from the focus of an X-ray zone plate. We note that in some circumstances, this configuration permits the formation of a direct solution for the phase [18].

In the work here we have modified a parallel ptychographic algorithm [19, 20] to allow an increased weight to be placed on more intense regions of the illumination. The reconstruction algorithm can be adapted for use with a number of iterative phase retrieval methods [21]. The algorithm first performs M CDI phase retrieval iterations on each phase diverse dataset, I^j, where $j = 1..N$. These iterations can use a variety of phase retrieval techniques. In a Fresel CDI (FCDI) geometry numerical simulations demonstrate that simple error reduction [5] produces similar results to more advanced algorithms such as difference map (DM) [22]. Following this, a new estimate of the transmission function is calculated via:

$$T_{k+1}(\boldsymbol{\rho}_s) = [1-\beta]T_k(\boldsymbol{\rho}_s) + \frac{\beta \sum_{j=1}^{N} \omega_j(\boldsymbol{\rho}_s) T_{k+1}^j(\boldsymbol{\rho}_s - \boldsymbol{\rho}_j)}{\sum_{j=1}^{N} \omega_j(\boldsymbol{\rho}_s)}$$

$$(2)$$

where β is the feedback parameter. This process is repeated for K iterations, where $k = 1..K$ is the current iteration number. The weighting factor $\omega_j(\boldsymbol{\rho}_s)$ is defined by the illuminating wavefield, $\psi_j(\boldsymbol{\rho}_s)$:

$$\omega_j(\boldsymbol{\rho}_s) = \alpha_j \left(\frac{|\psi_j(\boldsymbol{\rho}_s)|}{|\psi_j(\boldsymbol{\rho}_s)|_{MAX}}\right)^{\gamma} \qquad (3)$$

where γ is an amplification factor and α_j is the probe specific scaling factor, useful in situations where there is a notable variation in incident flux between probe positions. The set of parameters $\beta = 1$, $\alpha_j = 1$, $\gamma = 1$ reduces Eq. (2) to a typical parallel ptychographic algorithm [19, 20]. Numerical simulations demonstrate that in a Fresnel geometry using $\gamma \in [2:5]$ and $M = 1$ results in the most accurate reconstructions, based on the mean square error between the simulated, and reconstructed transmission functions. This error increased significantly for $1 > \gamma > 8$. $\beta = 1$ resulted in the lowest error in numerical simulations, implying all necessary feedback from previous iterations is already encapsulated in the right most term of Eq. 2. $\alpha = 1$ was chosen due to the equal incident flux and signal to noise for the measured data at each position.

The reliable convergence of the algorithm and the uniqueness of the solution obtained by Eq. 2 can be inferred from the uniqueness of the FCDI phase retrieval used within the algorithm [15], further strengthened by the addition of overlapping probe positions [10]. Deviation from the range of ideal parameters reduces the quality of the final reconstruction, irrespective of the convergence speed, which does not deviate appreciably. Phase diverse CDI is also compatible with diverging beam methods that use knowledge of the structure or composition of the sample to enhance reconstruction quality [23].

Diffraction data for a Au/Cr nano-structured test object was taken using a dedicated Fresnel imaging endstation situated at beamline 2-ID-B of the Advanced Photon Source, Argonne National Laboratory. Samples were mounted *in vacuo* on Si_3N_4 windows and illuminated with 2.5 keV X-rays under the Fresnel geometry [23], depicted in Fig.1a. A 160 μm diameter Fresnel zoneplate was used to impart phase and amplitude structure on the sample in the form of a diverging illumination.

Phase diverse CDI data for the Au/Cr object (shown in Fig. 2a) was obtained using both longitudinal and transverse phase-diversity in the illuminating wavefield. In total, 7 phase diverse positions (geometries depicted in Fig. 1b) were used to image the object. This included 4 different longitudinal positions ranging from $z_S = 1.8$ mm to $z_S = 2.2$ mm. For these longitudinal positions the diameter of the approximately circular illumination in the plane of the sample ranged from 15 μm to 20 μm. At each of the 7 positions 100 frames (each with a 1 second dwell time) were recorded using a 2048×2048 direct detection cooled CCD with 13.5 μm wide pixels. The overlap fraction for the translational phase-diversity measurements was between 50% and 85% [24]. Measurements of the unperturbed illumination were taken for each position and reconstructed using the method of Quiney et al. [25].
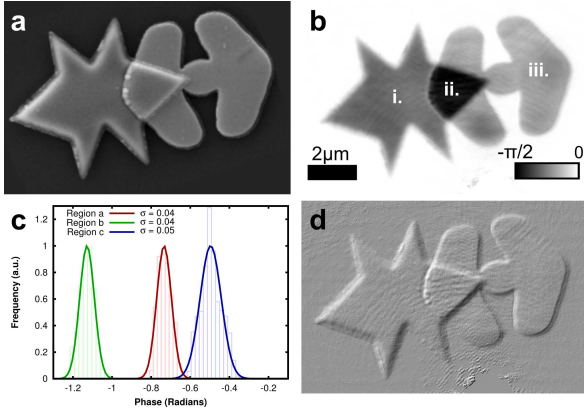
FIG. 2. (a) A scanning electron microscopy image of the nano-structured Au/Cr object. (b) Phase-diversity CDI reconstruction, showing the phase of the reconstructed transmission function. (c) Gaussian distributions were fitted to the recovered phase in regions i., ii., and iii., (shown in b). The watermarked regions in the plot show the histograms created from the measured data. (d) Differential intensity contrast image calculated using a relative illumination phase shift of $\phi = \frac{\pi}{2}$ and a translation of $\boldsymbol{\rho}_0 = (3.2, 3.2)$ μm.
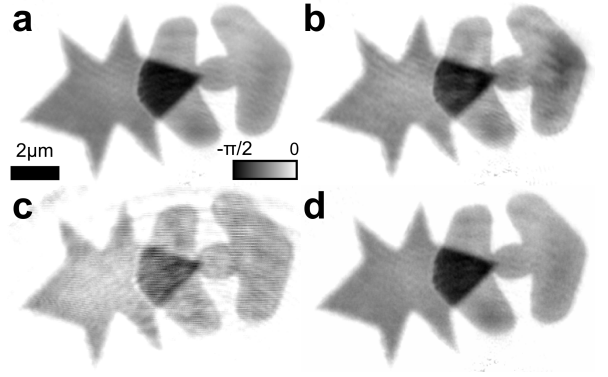

FIG. 3. A dose limited comparison of single probe measured images, and phase diverse reconstructions. The images show the phase of the reconstructed transmission function after 70 seconds of net exposure for (a), a phase diverse CDI reconstruction using both longitudinal and translational phase-diversity, (b) a phase diverse CDI reconstruction using translational phase-diversity, and (c), a single probe FCDI reconstruction. (d) Reconstructed phase using 7 seconds of net exposure for a phase diverse CDI reconstruction using both longitudinal and translational phase-diversity.

Image reconstructions were performed using the phase diverse CDI methodology summarised in Eq. 2. Fig. 2b shows the phase of the reconstructed transmission function of the nano-structured sample. The estimate of the spatial resolution of the image is based on analysis of the power spectrum of the reconstructed object, and was found to be approximately 45 nm. Here however, we are more concerned with matters of image contrast and sensitivity, which we define as "phase resolution", by which we mean the minimum phase step that can be clearly resolved in the image. This resolution is important in biological imaging for example, where subtle variations in cellular composition provide weak contrast mechanisms.

Phase resolution here is defined by measuring the standard deviation, σ, of a Gaussian fit to the recovered phase distribution, $\Delta\phi$, in a region of the sample known to be of uniform thickness. The value of σ, along with knowledge of the sample composition can then used to calculate a thickness resolution via $\Delta\tau = \Delta\phi/k\delta$.

The phase resolution for the nano-structured sample was estimated using the regions highlighted in Fig. 2b, which were verified to be of uniform thickness via atomic force microscopy. A phase resolution of $\Delta\phi = 0.04$ radians was calculated for the phase diverse reconstructions (histograms of phase distributions are shown in Fig. 2c).

In an Cr sample a phase resolution of $\Delta\phi = 0.04$ radians equates to a thickness resolution of 15 nm at 2.5 keV, calculated using tabulated data [26]. Similarly, in a proteinaceous sample, $\Delta\phi = 0.04$ radians implies a thickness resolution of $\simeq 50$ nm.

The phase and amplitude quantitatively recovered by coherent imaging methods allows for a great deal of flexibility in the contrast mechanisms used to display the re-

covered images [27]. A differential interference contrast (DIC) image for the nano-structured object was emulated by calculating the intensity of the exit wavefield from the sample when illuminated with two different wavefields, one of which is both phase shifted and translated [28]. The similarity between the emulated DIC image (Fig. 2d) and the measured scanning electron microscopy image (Fig. 2a) is obvious.

We now demonstrate the relative improvements of phase diverse CDI to a single probe FCDI reconstruction with an equal net absorbed X-ray dose. A comparison is also made using an equal X-ray dose while using only translational diversity. In this case the lateral beam overlap fraction was approximately 60% and an irregular arrangement of probe positions was used to minimise artefacts due to aliasing [29]. The sample was completely contained within the extent of the illuminating probe, hence the absorbed dose is equal to the cumulative dose contributed when recording the diffraction data.

A qualitative comparison of single probe FCDI, phase diverse CDI using lateral phase-diversity, and phase diverse CDI using both lateral and translational phase-diversity is shown in Fig. 3. This includes a reconstruction using phase diverse CDI with an order of magnitude less net exposure.

At an X-ray energy of $E = 2.5$ keV, the absorption coefficients for the Au and Cr components of the test sample are $\mu_{Au} = 4.86 \times 10^6$ m^{-1} and $\mu_{Cr} = 4.76 \times 10^5$ m^{-1} respectively. Based on estimates of detector gain and measurements of the unperturbed illumination, the incident photon flux was determined for each phase diverse position used in the reconstructions. This information was used to estimate the absorbed X-ray dose to each region of the sample [30].

Data Set	Exposure Time	Cr Absorbed Dose (Gy)	Cr Phase Resolution
Phase Diverse (long. + trans.)	70 s	6.5×10^5	0.04
Phase Diverse (trans.)	70 s	6.7×10^5	0.07
Single Position	70 s	6.9×10^5	0.12
Phase Diverse (long. + trans.)	7 s	6.5×10^4	0.05

TABLE I. The absorbed X-ray dose (for the Cr region of the sample) used to obtain each of the reconstructions in Fig. 3. Minor variations in absorbed dose were due to temporal beam fluctuations.

The absorbed dose corresponding to each of the reconstructions in Fig. 3 is shown in Table I, demonstrating a 3× increase in phase resolution when an equal dose is applied. A phase diverse measurement with 10% of the dose of a single probe measurement still displays a factor of 2 improvement in phase resolution. This allow us to conclude that the phase diverse method here allows an order-of-magnitude decrease in radiation dose whilst yielding significantly improved image contrast and negligible loss of spatial resolution. One must still pay careful attention to the desired spatial (lateral) resolution in the reconstruction, as this figure is closely related to the absorbed radiation dose for diffraction imaging [30].

The application of phase-diversity, in particular the use of longitudinal diversity, has shown significant increases in phase resolution with a corresponding decrease in artefacts compared to other approaches using a diverging illumination [20]. With longitudinal diversity our results approach the level of sensitivity required to discern subtle variations in the internal structure of materials and organic samples. We have shown that by distributing the dose over a range of different forms of illumination it is possible to reliably form very high quality images. Indeed, for a given image quality, phase-diversity offers a substantial reduction in the imaging dose required. The method has broad potential for application in X-ray and electron imaging.

[1] K.A. Nugent, Adv. Phys. **59**, 1 (2010).
[2] L. De Caro, E. Carlino, G. Caputo, P.D. Cozzoli, et al., Nat. Nano. Tech. **5**, 360 (2010).
[3] R.H.T. Bates, Optik **61**, 247 (1982).
[4] D. Sayre, Acta Crystallogr. **5**, 843 (1952).
[5] J.R. Fienup, Appl. Optics **21**, 2758 (1982).
[6] B. Abbey, G.J. Williams, M.A. Pfeifer, J.N. Clark, et al., App. Phys. Lett. **93**, 214101 (2008).
[7] B. Abbey, K.A. Nugent, G.J. Williams, J.N. Clark, et al., Nat. Phys. **4**, 394 (2008).
[8] R. Hegerl and W. Hoppe, Ber. Bunsen Ges. Phys. Chem. **74**, 1148 (1970).
[9] H.N. Chapman, Ultramicroscopy **66**, 153 (1996).
[10] J.M. Rodenburg and H.M.L Faulkner, App. Phys. Lett. **85**, 4795 (2004).
[11] R.G. Paxman, T.J. Schulz, and J.R. Fienup, J. Opt. Soc. Am. A **9**, 1072 (1992).
[12] P. Cloetens, W. Ludwig, J. Baruchel, D. Van Dyck, et al., App. Phys. Lett. **75**, 2912 (1999).
[13] W. Coene, G. Janssen, M. Op de Beeck, and D. Van Dyck, Phys. Rev. Lett. **69**, 3743 (1992).
[14] K.A. Nugent, A.G. Peele, H.N. Chapman, and A.P. Mancuso, Phys. Rev. Lett. **91**, 203902 (2003).
[15] K.A. Nugent, A.G. Peele, H.M. Quiney, and H.N. Chapman, Acta Crystallogr. A **61**, 373 (2005).
[16] C.T. Putkunz, M.A. Pfeifer, A.G. Peele, G.J. Williams, et al., Opt. Express **18**, 11746 (2010).
[17] M. Guizar-Sicairos and J.R. Fienup, Opt. Express **16**, 7264 (2008).
[18] H.M. Quiney, G.J. Williams, and K.A. Nugent, Opt. Express **16**, 6896 (2008).
[19] P. Thibault, M. Dierolf, A. Menzel, O. Bunk, et al., Science **321**, 379 (2008).
[20] D.J. Vine, G.J. Williams, B. Abbey, M.A. Pfeifer, et al., Phys. Rev. A **80**, 063823 (2009).
[21] H.M. Quiney, J. Mod. Optics **57**, 1109 (2010).
[22] V. Elser, J. Opt. Soc. Am. A **20**, 40 (2003).
[23] J.N. Clark, C.T. Putkunz, M.A. Pfeifer, A.G. Peele, et al., Opt. Express **18**, 1981 (2010).
[24] O. Bunk, M. Dierolf, S. Kynde, I. Johnson, et al., Ultramicroscopy **108**, 481 (2008).
[25] H.M. Quiney, A.G. Peele, Z. Cai, and Nugent K.A. Paterson, D., Nat. Phys. **2**, 101 (2006).
[26] B.L. Henke, E.M. Gullikson, and J.C. Davis, Atomic Data and Nuclear Data Tables **54**, 181 (1993).
[27] D. Paganin, T.E. Gureyev, S.C. Mayo, A.W. Stevenson, et al., J. Microsc. **214**, 315 (2004).
[28] E.D. Barone-Nugent, A. Barty, and K.A. Nugent, J. Microsc. **206**, 194 (2002).
[29] M. Dierolf, P. Thibault, A. Menzel, C.M. Kewish, et al., New J. Phys. **12**, (2010).
[30] M.R. Howells, T. Beetz, H.N. Chapman, C. Cui, et al.,